Draft version November 10, 2015
Preprint typeset using LaTeX style emulateapj v. 5/2/11

arXiv:1511.02280v1 [astro-ph.HE] 7 Nov 2015

FERMI-LAT OBSERVATIONS OF 2014 MAY–JULY OUTBURST FROM 3C 454.3

Richard J. G. Britto[1], Sara Buson[2,3,4,5], Benoît Lott[6], Soebur Razzaque[1] and Eugenio Bottacini[7]

Draft version November 10, 2015

ABSTRACT

A prominent outburst of the flat spectrum radio quasar 3C 454.3 was observed in June 2014 with the *Fermi* Large Area Telescope. This outburst was characterized by a three-stage light-curve pattern—plateau, flare and post-flare—that occurred from 2014 May to July, in a similar pattern as observed during the exceptional outburst in 2010 November. The highest flux of the outburst reported in this paper occurred during 2014 June 7–29, showing a multiple-peak structure in the light-curves. The average flux in these 22 days was found to be $F[E > 100\ \mathrm{MeV}] = (7.2 \pm 0.2) \times 10^{-6}$ ph cm^{-2} s^{-1}, with a spectral index, for a simple power law, of $\Gamma = 2.05 \pm 0.01$. That made this outburst the first γ-ray high state of 3C 454.3 to be ever detected by *Fermi* with such a hard spectrum over several days. The highest flux was recorded on 2014 June 15, in a 3-hr bin, at MJD 56823.5625, at a level of $F[E > 100\ \mathrm{MeV}] = (21.6 \pm 2.6) \times 10^{-6}$ ph cm^{-2} s^{-1}. The rise time of one of the short subflares was found to be $T_r = 1000 \pm 500$ s at MJD=56827, when the flux increased from 4 to 12 $\times 10^{-6}$ ph cm^{-2} s^{-1}. Several photons above 20 GeV were collected during this outburst, including one at 43 GeV on MJD 56827, constraining the γ-ray emission region to be located close to the outer boundary of the broad-line region (BLR), leading to fast flux variability.

Subject headings: galaxies: active - γ rays: galaxies - quasars: individual (3C 454.3)

1. INTRODUCTION

The flat spectrum radio quasar (FSRQ) 3C 454.3 (also cataloged as PKS 2251+158; R. A.=22h 53m 57.748s, Decl.=+16° 08′ 53.56″ (2000); redshift z=0.859 (Lynds 1967)) is a well-known active galactic nucleus (AGN) that shows very bright flaring activity across the electromagnetic waveband. The source was detected above 100 MeV by the *Energetic Gamma Ray Experiment Telescope (EGRET)* on board the *Compton Gamma Ray Observatory* in 1999 (Hartman et al. 1999). Flares were reported by the *AGILE* space telescope since 2007 (Vercellone et al. 2009, 2010) and by the *Fermi* Large Area Telescope (*Fermi*-LAT) since 2008 (Abdo et al. 2009). Four historical flaring episodes made 3C 454.3 the brightest γ-ray source ever recorded in the sky, apart from γ-ray bursts, and were studied in detail using *Fermi*-LAT data. These outflows occurred in 2009 December (Striani et al. 2010; Ackermann et al. 2010), 2010 April (Ackermann et al. 2010), 2010 November (Abdo et al. 2011) and 2014 June (this work). The daily recorded flux levels detected by *Fermi*-LAT, $F[E > 100\ \mathrm{MeV}]$ (F_{100}, in units of 10^{-6} photons cm^{-2} s^{-1}), reached $F_{100} = 22 \pm 1$ in 2009 December and $F_{100} \simeq 16$ in 2010 April (Striani et al. 2010; Ackermann et al. 2010). In 2010 November, the source displayed sustained activity at a level of $F_{100} \simeq 10$ for several days, and then showed a fast rise to $F_{100} \simeq 55$, before reaching the historic record level of $F_{100} \simeq 80$ in a 6-hr bin, on 2010 November 20 (Abdo et al. 2011).

The 2009-2010 outbursts of 3C 454.3 exhibit similar patterns including three phases, which was more clearly observable in the light-curve of the 2010 September-December outburst (Abdo et al. 2011). First, there is a plateau phase at the beginning where the flux rapidly increases and remains steady for a few days at a relatively high state, followed by the main flare (that usually exhibits several distinct peaks). A post-flare phase is then visible, where the flux is more or less fluctuating at a lower level than the flare, but generally at a higher level than the plateau. This three-phase pattern was first identified and reported in Ackermann et al. (2010) and Abdo et al. (2011), and then quantitatively described in Jorstad et al. (2013), for the three 2009-2010 outbursts. It is also common to present data of a quiescent phase (referred to as *pre-flare*), preceding the plateau, for comparative studies with the following high-state activity.

A significant hardening of the photon index Γ was reported during the 2010 November outburst (Abdo et al. 2011). For $E > 100$ MeV and a power-law (PL) model, $\Gamma \simeq 2$ was measured during this flare in 6-hr bins, compared to $\Gamma \simeq 2.5$ in the quiescent regime. An even harder index has been reported during the short flare of 2013 September 23-25, when $\Gamma \simeq 1.82 \pm 0.06$ was measured up to 40 GeV, on average during those two days (Pacciani et al. 2014).

Like many other bright FSRQs, 3C 454.3 shows a spectral break at GeV energies, which was found to be almost independent of its flux level (Abdo et al. 2010). A change in the power-law photon index was reported to be signif-

[1] Department of Physics, University of Johannesburg, Auckland Park 2006, South Africa, *rbritto@uj.ac.za, srazzaque@uj.ac.za*
[2] *Istituto Nazionale di Fisica Nucleare, Sezione di Padova, I-34131, Padova, Italy*
[3] *Dipartimento di Fisica "G. Galilei", Università di Padova, I-34131, Padova, Italy*
[4] *Current affiliation: Astrophysics Science Division, NASA Goddard Space Flight Center, Greenbelt, MD 20771 USA,* sara.buson@nasa.gov
[5] Current affiliation: University of Maryland Baltimore County/CRESST, Baltimore, MD 21250, USA
[6] Univ. Bordeaux, Centre d'Études Nucléaires de Bordeaux-Gradignan, UMR 5797, CNRS/IN2P3, 33175 Gradignan, France, *lott@cenbg.in2p3.fr*
[7] *W. W. Hansen Experimental Physics Laboratory, Stanford University, Stanford, CA 94305, USA*

icantly more than one unit at energies around 2 GeV (Abdo et al. 2009; Ackermann et al. 2010; Abdo et al. 2011). As this spectral feature was not a theoretical prediction and was observed only with *Fermi*-LAT from 2008, different models were proposed only in recent years, to account for it. Indeed, this broken spectrum was found inconsistent with a γ-ray photon distribution produced by inverse-Compton (IC) scattering due to a cooling electron distribution. Finke & Dermer (2010) proposed a combination of the Compton-scattered disk and broad-line region (BLR) radiation to explain the spectral break and also fit the quasi-simultaneous radio, optical/UV, X-ray and γ-ray spectral energy distributions (SEDs), using data from the 2008 August flare. Also, Cerruti et al. (2013) proposed that the break feature can be explained by a log-parabolic distribution of non-thermal electrons that up-scattered photons in the BLR, using data from both the 2008 August and the 2010 November flares. By studying the effect of a continuous time-dependent particle injection of electrons into the jet, Hunger & Reimer (2015) proposed a phenomenological model-independent approach which was applied to the 2010 November flare. They found that the combination of the Compton-scattered disk and BLR radiation, and the Compton-scattered BLR radiation only with an intrinsic break in the ambient particle distribution, are both viable scenarios, for specific injection parameters. More recently, Kohler & Nalewajko (2015) studied short bright γ-ray flares of several blazars, including 3C 454.3, and report variable spectral features that significantly depart from the average spectrum that is obtained over several months/years. They suggest that the average *Fermi*-LAT spectrum does not reflect a specific particle acceleration scenario, since it appears to be the superposition of several short-lived components, each one exhibiting a different spectral curvature. The observed SEDs would rather reflect macroscopic turbulence in relativistic jets with emitting regions having a narrow energy distribution of emitting particles.

Exotic scenarios such as mixing of photons with axion-like particles in the large-scale jet has also been found to fit the spectra of 3C 454.3 in its 2010 November outburst (Mena & Razzaque 2013).

Another important issue that is investigated in the study of FSRQs, in connection with the GeV spectral break, is the location of the γ-ray emission region. Observations at GeV energies could constrain the location of the emission region to be within or beyond the BLR (Dotson et al. 2012; Orienti et al. 2013; Nalewajko et al. 2014). More specifically, for each flare, different attempts were made to constrain the location of the γ-ray emitting blob. Fuhrmann et al. (2014) performed radio/γ-ray correlation studies of 54 bright *Fermi* blazars, including 3C 454.3, on a 3.5-yr data sample. Based on a discrete cross-correlation function analysis method, they measured time lags between light-curves at different frequencies and the γ-ray light-curve, constraining the γ-ray emitting region to lie between 0.8-1.6 pc from the super massive black hole (SMBH) for 3C 454.3. For the same source, the 3 mm $\tau = 1$ optical depth surface is found to lie between 2-3 pc from the SMBH, which is higher than the typical bulk BLR radius of $\sim$ 0.2 pc for this source. This would suggest that γ rays are produced beyond the canonical BLR and that some material of the BLR also lies at these larger distances. However, it is also interesting to study the steady γ-ray emission over a long period of time, as performed by Poutanen & Stern (2010). These authors have presented studies from 180 days of *Fermi*-LAT data to model the spectral breaks, using the pair production mechanism from γ rays of the jet interacting with UV photons of the BLR. In Stern & Poutanen (2011), they propose a model for 3C 454.3 (data collected in 2008-2011) in which γ rays are produced close to the boundary of the high-ionization part of the BLR, and move away from the black hole with the increase of the flux. In their latest study of 1740 days of *Fermi*-LAT data from bright blazars, they propose that a $\sim$5 GeV break is mainly due to He II Ly continuum photons at 54.4 eV, and that a $\sim$20 GeV break is mainly due to H Ly continuum. In the case of 3C 454.3, these would give a significant constraint on the location of the γ-ray emission region to be within the BLR (Stern & Poutanen 2014).

A multiwavelength study of 3C 454.3 data obtained during the period 2005-2008 was performed by Jorstad et al. (2010), reporting correlation between optical, X-ray and γ-ray variations, and proposing that the γ-ray emission is dominated by the external Compton (EC) mechanism. Pacciani et al. (2010) used the November–December 2009 multiwavelenghth campaign data on the bright flare of 3C 454.3 to model the pre– and post flare broadband SED with a one-zone synchrotron self-Compton plus EC emission model. However, they determined that the SED around flare maximum required an additional particle component to achieve a satisfactory fit. On the other hand, the study of the same 2009 December flare by Bonnoli et al. (2011) led them to the conclusion that a simple one-zone synchrotron + IC emission can model the broadband SED, the IC emission consisting of synchrotron self-Compton in the X-ray band, in addition to EC.

In this paper we report on the 2014 May–July outburst of 3C 454.3 as observed by *Fermi*-LAT. Although the flux (F_{100}) during this latest outburst did not reach the level of the 2010 November flare, it lasted longer and we could separate its different substructures quite well, compared to the previous flares. This flare was reported by AGILE first in Verrecchia et al. (2014) during its plateau phase. We also observed that the flux remained quite high (very often at $F_{100} > 2$ daily) for several weeks after the flare. The plateau–flare–post-flare pattern was clearly observed as well. During this outburst, a spectrum significantly harder than in 2010 was measured, with most of the flaring phase being observed with a hard photon spectral index $\Gamma \simeq 2$, mainly during the MJD 56828.0-56833.5 period. To the best of the authors' knowledge, this is the first γ-ray high state of 3C 454.3 to be ever detected with such a hard power law photon index, except for the September 2013 flare that was too short to be characterized in detail in its temporal as well as its spectral structure (Pacciani et al. 2014). The tendency of a "harder when brighter" pattern for 3C 454.3 was clearly visible during this (2014) outburst, when comparing the spectral shape of the different phases.

We study flux variability and change in spectral properties in the γ-ray band at different epochs during the 2014 May–July outburst of 3C 454.3. Detection of a flux rise time of $\sim$1000 seconds in one of the short dura-

tion subflares is one of the shortest in the GeV band for 3C 454.3. A 43 GeV photon was detected with high confidence during this subflare, allowing us to put a lower limit on the jet Lorentz factor that is the highest to date along with what was estimated by Sikora et al. (2008). Another high-energy, 35 GeV, photon was also detected during this outburst.

X-ray, optical and near infrared light-curves were seen to be well correlated with the *Fermi*-LAT γ-ray data during this latest flare, though the radio light-curve shows a global tendency of continuous increase during the main outburst structure (Carrasco et al. 2014; Chandra et al. 2014; MacPherson et al. 2014). Tachibana et al. (2015) reported the analysis of optical versus γ-ray data in the MJD 56800-56910 period, showing some evidence of a change in the Doppler factor δ during the flare.

In Section 2, observations and analysis of *Fermi*-LAT data for the outburst phases are presented, including light-curves, high energy ($\gtrsim$ 10 GeV) photons and γ-ray luminosities, fastest variability studies and SEDs. In section 3, we present the analysis of *Swift*-XRT data. Results are presented in Section 4 and Discussion in Section 5. A flat Λ-CDM cosmology with $H_0 = 69.6$ km s^{-1} Mpc^{-1}, $\Omega_m = 0.286$, and $\Omega_\Lambda = 0.714$ is used in this paper (Planck Collaboration et al. 2014).

2. *FERMI*-LAT OBSERVATIONS AND ANALYSIS

The *Fermi*-LAT is a pair-conversion γ-ray telescope sensitive to photon energies greater than 20 MeV with a field of view of about 2.4 sr (Atwood et al. 2009). The data presented in this paper were collected during the 2013 Oct 05-2014 Jul 25 period (MJD 56570.0 to 56863.0). During this phase, in contrast to the nominal scanning mode where the LAT surveys the whole sky every 3 hr, different Target of Opportunity-motivated, modified observing modes enhancing the exposure of PSR B1259-63 were in place. Also, due to an instrument pointing issue, no data were collected on the whole sky during a ∼13-hr long period (MJD 56834.07–56834.65) leading to a gap in the light-curves shown below (corresponding to the "peak 6" phase).

Only photons with energies greater than 100 MeV were considered in this analysis. In order to avoid contamination from the Earth limb γ rays, a selection of events with zenith angle $\theta_z = 100°$ was applied. This analysis was performed with the standard analysis tool *gtlike/pyLikelihood*, which are part of the *Fermi* Science Tools software package (version v9r33p0)[8]. The P7REP_V15_SOURCE set of instrument response functions (IRFs) was used. We selected Pass 7 reprocessed source-class events above 100 MeV. Compared to the Pass 6 analyses of previous outbursts of 3C 454.3 presented in Ackermann et al. (2010) and Abdo et al. (2011), our setup provides a higher effective area below 200 MeV and a better angular resolution above a few GeV, in addition to improved models for the diffuse emission components (Ackermann et al. 2012; Bregeon et al. 2013).

In the analysis presented in this paper, photons were selected in a 10° circular region of interest (ROI), centered at the position of 3C 454.3. The isotropic background, including the sum of residual instrumental background and extragalactic diffuse γ-ray background, was modeled by fitting this component at high Galactic latitude (file "iso_source_v05.txt" provided with the *Fermi Science Tools*). The "gll_iem_v05_rev1" Galactic diffuse emission model was used (the Galactic longitude and latitude of 3C 454.3 are 86°.1 and 38°.2, respectively). All point sources in the third *Fermi*-LAT source catalog (3FGL, (Acero et al. 2015)) located in the ROI and an additional surrounding 10° wide annulus (called "source region") were modeled in the fits, with the spectral parameters kept free only for the brightest sources in the ROI. Depending of the type (spectral or time domain) of analysis, either two or four point sources responded to the criteria of "brightest sources", corresponding to a detection significance in 3FGL having a TS of at least 20.

The source variability was investigated by producing light-curves with various time bins (1 day, 6 hr, 3 hr), and using an unbinned method for the study of fastest variability. Although spectral breaks and curvatures were found to be characteristics of the actual spectral shape of 3C 454.3, light-curves were produced by modeling the spectra in each time bin as a simple PL over the 0.1-300 GeV energy range, since the statistics in these narrow time bins is not enough to significantly favor spectral shapes more complex than PL. Also, the statistical uncertainties of the photon indices obtained from PL fitted models are smaller than those obtained from these more complex functions (Ackermann et al. 2010). The PL fit function used in the *unbinned likelihood* procedure is defined in the following paragraph.

Spectral analysis has been processed over several epochs of the flaring activity and fits were performed over the 0.1-500 GeV range, using the unbinned likelihood analysis package. The four following functions were successively used in our analysis:

- a *power law (PL)*, defined as

$$dN(E)/dE = N_p \ (E/E_p)^{-\Gamma}, \tag{1}$$

  with $E_p = 412.7$ MeV, which is the value of the pivot energy given in 3FGL;

- a *broken power law (BPL)*, defined as

$$dN(E)/dE = N_0 \ (E/E_{break})^{-\Gamma_i}, \tag{2}$$

  with $i = 1$ if $E < E_{break}$ and $i = 2$ if $E > E_{break}$;

- a *log-parabola (LP)*, defined as

$$dN(E)/dE = N_0 \ (E/E_0)^{-\alpha-\beta \ \ln(E/E_0)}, \tag{3}$$

  with $E_0 = 297.6$ MeV, which is the value of the pivot energy of the *LP* spectral fit of 3C 454.3 as reported in the *Second* Fermi-*LAT source catalog (2FGL)* in Nolan et al. (2012), and where "ln" is the natural logarithm;

- a *power law with an exponential cutoff (PLEC)*, defined as

$$dN(E)/dE = N_0 \ (E/E_p)^{-\Gamma} \ \exp(-E/E_c), \tag{4}$$

  with $E_p = 412.7$ MeV (as for the PL).

[8] http://fermi.gsfc.nasa.gov/ssc/data/analysis/software/

The estimated systematic uncertainty on the effective area is 10% at 100 MeV, 5% in the 316 MeV-10 GeV range, and 15% at 10 GeV. The energy resolution is between 10 and 20% over the 0.1-1 GeV range, and less than 10% over the 1-100 GeV range.

3. *SWIFT*-XRT ANALYSES

During the 2014 June outburst revealed by the LAT, five *Swift*-XRT observations of 3C 454.3 were performed in two observation modes: Photon Counting (PC) mode and Windowed Timing (WT) mode. Table 1 reports the observation log.

Observations were analyzed using `xrtproducts` and *HEAsoft 6.15*. For the analysis, events were extracted from a circular region of interest centered on the source position having a radius of ∼20 pixels (that corresponds to ∼47 arcsec, Moretti et al. 2004). The background is computed from a source-free nearby region having a radius of ∼50 pixels. Spectral data were grouped to a minimum of 20 counts per energy bin that allows us to confidently use the chi-square statistic.

In our spectral analysis approach, we first fit the spectra with the simplest model, which is a power law keeping the absorption fixed to the Galactic value (N_H^{gal} = 6.63 × 10^{20} atoms cm^{-2}). This value is derived from the LAB Survey of Galactic HI database (Kalberla et al. 2005). If the fit result can be improved with more sophisticated models, we estimate its significance with the F-test (Bevington & Robinson 1992). As a result we find that none of the spectra require absorption in addition to the Galactic value. This also excludes variable absorption for 3C 454.3 because we have analyzed data from five different epochs. In more detail, observations 00031018014, 00031018016 and 00031018017 are best modeled by a power law. Instead a broken power law best reproduces the spectra of observations 00031018019 and 00031018020. A simple power-law model applied to these two observations leads to a fit result of χ^2 = 88.98 / 69 d.o.f. for the former and χ^2 = 183.14 / 135 d.o.f. for the latter observation. By applying the F-test the result shows that the spectral fit improvement obtained by using the broken power-law model with respect to the simple power law is not due to chance. The spectra were analyzed with XSPEC 12 (Arnaud 1996). The fitting was performed over the energy band 0.6 – 6.0 keV. Fluxes are computed in the 2.0 – 6.0 keV energy range. All errors are presented at 90% CL. The results are shown in Table 1.

4. RESULTS

In this section, we report on variability studies and spectral analysis of 3C 454.3 during the outburst phase of 2014 May–July (plateau, flare, post-flare), as well as during the "pre-flare" quiescent phase preceding the outburst.

4.1. *light-curves*

The characteristic temporal evolution of the flux of 3C 454.3 during its May–July outburst can be identified by a three phase pattern (plateau, flare and post-flare), as described in the introduction. We show in Fig. 1 a 1-day light-curve encompassing the pre-flare and the three-phase outburst. These phases are described in Table 2. A pre-flare phase was observed, from MJD 56570 to 56797, during which the flux remains, for most of the time, below $F_{100} = 2$. This phase started after the 23–25 September 2013 outflow, and lasted for 227 days. Analysis of the pre-flare data is used to show the spectral behavior and flux level during the quiescent phase of the source. A plateau phase was then observed from MJD 56797 to 56815, during which the flux rose slightly and remained quite stable. During the flare phase, from MJD 56815 to 56837, the flux rose dramatically and exhibited a complex, structured trend. A post-flare phase was observed, during which the flux was at a higher level than the plateau phase and remained fluctuating. We define the post-flare phase between MJD 56837 to 56863, before secondary outbursts show up again. Indeed, 3C 454.3 remained in a relatively high state for several weeks after this outburst episode. In this study we also present a more detailed analysis of the flaring phase by scanning subflares on shorter time-scales.

Besides the flux evolution that defines an outburst, a spectral evolution is also observed, mainly characterized by a hardening of the photon spectral index (PL fitting), and detection of high-energy photons (> 10 GeV). The photon indices and high energy photons are displayed respectively in the middle and lower panels of Fig. 1. A significant hardening of the photon spectral index is observed when the flux increases, with values of Γ going below 2 during some parts of the flare. More precisely, we can report, from the 3-hr binned light-curve in Fig. 2, that the photon index $\Gamma < 2$ for 75 % of the time bins of Peak 4. We also report that $\Gamma < 2$ for ∼40 % of the time bins of Peak 5, mainly occurring during the second half of the peak.

In order to probe the flaring pattern over the whole flare phase (MJD 56815.0-56837.0) and to isolate subflaring events, we performed fits over different peaks observed in the 3-hr light-curve (Fig. 2). The highest flux is reached during MJD 56823 (maximum of Peak 3), with the value $F_{100} = 21.6 \pm 2.6$, associated with PL index $\Gamma = 2.1 \pm 0.1$, in a 3-hr bin, at 56823.5625. Measurement in a 6-hr bin was found to be $F_{100} = 19.4 \pm 1.7$, associated with PL index $\Gamma = 2.1 \pm 0.1$, at 56823.3750. Note that the hard spectra with $\Gamma < 2$ are observed at the end of Peak 4, 5 and 6. The lowest value of the photon index measured in a 6-hr bin was $\Gamma = 1.78 \pm 0.10$, at MJD 56834.125. Similar values ($\lesssim 1.8$) were also obtained in 3-hr bins, at MJD 56832.0625, 56827.6875, 56832.9375, 56834.0625, 56836.4375 and 56836.6875.

Through a detailed observation of the 3-hr light-curve we can identify nine individual flaring structures with a flux above $6 \times 10^{-6} ph\ cm^{-2} s^{-1}$. We fitted these nine peaks in order to account for the whole light-curve pattern over the MJD 56814.5-56835.1 range, in addition to a constant function to represent the baseline flux. Each of the 9 fits were performed using the following function:

$$F = 2F_0 (e^{(t_0 - t)/T_r} + e^{(t - t_0)/T_f})^{-1}, \quad (5)$$

where:

- t_0 is the time of the peak value;
- T_r and T_f are the rise and fall time, respectively;
- F_0 is the flux at t_0, representing the subflare amplitude

However, in the following discussions, we will only consider the six major peaks indicated in Fig. 2. From our best fit model, we obtained a rise time $T_r = 0.04 \pm 0.02$ day ($\sim$ 1 hr $\pm$ 30 min), associated with Peak 4, centered at t_0=56827.125, though the large statistical error associated with this parameter allows significantly different values. Peaks 2 and 5 are the broadest peaks, both reaching $F_{100} \simeq 16 \pm 2$ with their T_r and T_f of the order of one day. Peak 1 and Peak 4 are the objects of a more detailed study in Section 4.3, when we investigate the fastest variability pattern.

We also observe in Fig. 2 more detail about the variation of the photon index during the flare. The "Flare I" and "Flare II" labels identify the two major subflares that will be studied in more detail later in this section, and that we have already defined in Table 2. Time ranges of Peaks 2, 4 and 5 are indicated by dashed/dotted vertical lines.

For the four spectral models defined in Section 2, the total integrated flux (F_{100}) has been computed for each phase of the outburst (1, 2, 3, 3a, 3b, 4) and for Peaks 2, 4 and 5 already mentioned. We show in Fig. 3 the plots of the dependence of the photon spectral index Γ on the flux for phases 1, 2, 3a, 3b and 4, for the PL fit (left panel) and BPL fit (right panel). The "harder when brighter" spectral property we already mentioned is clearly observable through these different phases of the outburst.

We searched for some time dependent or geometrical pattern of the "photon index *versus* Flux[$> E_0$]" graphs for Peaks 2, 3 and 4, in both 6-hr and 12-hr binning for each peak respectively, but we could not find any obvious one, the "harder when brighter" tendency being only partially observed in such narrow time intervals.

4.2. *High-energy photons and peak luminosity*

A harder spectral index associated with the detection of high energy photons during the flare and post-flare phases seems to be a common feature of high-state activity for 3C 454.3.

In the bottom panel of both Fig. 1 and 2 are presented the high energy (HE) photons above 10 GeV along with the light-curves. To identify γ-ray induced events with a high degree of accuracy, we use the "ULTRACLEAN" class of events. We report events at energies E$>$ 10 GeV, along with their arrival time and a probability $>$0.9545 (2-σ Gaussian equivalent) to be associated with 3C 454.3, within a ROI = 0.5°. The way HE photons are distributed during the flare phase (phase 3) is clearly visible in Fig. 2. Most of the HE photons are detected during the second part of this phase, mainly after Peak 3. No HE photons were detected during Peak 1. Moreover, the bulk of HE photons is detected in the second half of the broad structures, like in both the Peak 2-Peak 3 and Peak 5 subflares. Around the maximum of Peak 5, we found one photon at E=34.6 GeV (MJD 56830.7616) with a probability 0.99999, and around the maximum of Peak 4, one photon at E=43.3 GeV (MJD 56827.1233) with a probability 0.99998.

In section 4.1 we presented studies of the flaring pattern of Peaks 2, 3, 4, and 5, as shown in Fig. 2. In Table 4 are presented spectral analysis along with estimation of the γ-ray luminosity corresponding to these integrated subflare phases.

The luminosity of the source was calculated for each of the three spectral shapes (BPL, LP and PLEC). Since we found photons up to 40-60 GeV energy bin in the analysis of 6 years of 3C 454.3's data (Britto et al. 2015), we chose to calculate the luminosity L in the 0.1-60 GeV energy range. This integrated apparent isotropic luminosity L was calculated according to the following formula:

$$L = 4\pi d_L^2 \int_{E_1(1+z)}^{E_2(1+z)} E \frac{dN(E)}{dE} dE, \qquad (6)$$

with E_1=100 MeV, E_2=60 GeV, the luminosity distance $d_L = 5.55$ Gpc $= 1.71 \times 10^{28}$ cm, using the cosmological parameters defined in Section 1, and $dN(E)/dE$ the differential form of the spectral model we have used. The highest values of the luminosity are found for Peak 3, at $L \simeq 30 \times 10^{48}$ erg s^{-1}.

4.3. *Fastest variability*

Some flares visible in the light-curves of Fig. 2 exhibit characteristic times commensurate with or shorter than the orbiting period of the Fermi satellite (1.5 hr). The standard analysis whereby the photons are binned in time is inappropriate for a detailed temporal characterization of these flares. In survey mode, a typical source is seen by the LAT only 20% of the survey period, T$_{surv}$, which is twice the orbiting period. The shortest time-binning commonly used in light-curves is T$_{surv}$ to avoid explicitly dealing with LAT's discontinuous exposure pattern, but the reliability of the so-obtained timescales is questionable when they are significantly shorter than the bin size. Instead of the standard analysis, we have used a maximum-likelihood approach (described in the context of the adaptive-binning method, ABM, in Lott et al. (2012)) where a time-dependent function is fitted to the unbinned data (*i.e.*, neither binned in time nor in energy).

We used a function of the form $S_S(E,t) = S(E) \times (F(t) + B)$, where $F(t)$ is given in Eq. 5, B is a continuous component and $S(E)$ is a power-law distribution (with fixed photon index, hence neglecting the spectral changes during the flare). To compute the likelihood, the needed instantaneous exposure rate was interpolated from the values assessed every 30 s (same time steps as in the spacecraft data file provided by the *Fermi Science Support Center*). In this section, we focus on the Peak-1 and -4 flares as they can be better characterized than the other fast flares.

Fig. 4 left panel displays different features concerning the MJD 56816 ("Peak 1") flare. The top panel displays the LAT exposure rate for 3C 454.3. The bottom panel shows the 3-hr and 6-hr light-curves as well as the function fitted on the 3-hr points (black) and the function resulting from the fit by the unbinned method (red). To enable a verification of the fit quality, a comparison between the counts of photons ascribed to the source between the data (blue) and the estimate from the fitted function (red) is given in the middle panel. The unbinned method gives T_r=3.8$\pm$1.1 ks (1.06 $\pm$ 0.31 hr), T_f=17$\pm$4 ks (4.72 $\pm$ 1.11 hr) in good agreement with the results of the conventional fit, but with better-defined uncertainties. For the MJD 56827 flare ("Peak 4"), the unbinned method yields T_r=1.0$\pm$0.5 ks (0.28 $\pm$ 0.14 hr) and T_f=24$\pm$4 ks (6.67 $\pm$ 1.11 hr). T_r in Peak 4 is the

shortest timescale reported for this source in the γ-ray band. Unexpectedly, this flare peaks in flux almost exactly simultaneously with a change in scanning mode. The accuracy and robustness of the analysis have been checked with Monte-Carlo simulations, and we verified that Peak 4 is not influenced by the change in scanning mode. Inspection of the data did not reveal any change in background during this flare that could have biased our results. The 43-GeV photon mentioned in section 4.2 was detected at MJD 56827.1233, *i.e.*, 4.5 ks (1.2 h) after the flux peak.

4.4. *Time-resolved SEDs*

The 2014 June outburst is less intense than the 2009 December and 2010 November outbursts, and reached a flux level similar to the 2010 April outburst. During these previous flaring activities, evidence of some hardening of the photon spectral index was found. The 2-day flare of 23-25 September 2013 was below F_{100}=4. However, a harder index $\Gamma \simeq 1.8 \pm 0.1$ was reported in Pacciani et al. (2014). The observation and study presented in the previous sections showed that the 2014 May–July outburst also exhibited a dramatic hardening of the photon index. In this section we focus on the SED studies, and report spectral features that characterized the different phases/subphases of the outburst.

We have performed the spectral analysis of the three phases of the 2014 May–July outburst, as well as the quiescent phase that preceded them, and separately the Flare I and Flare II phases (Table 2), in the 0.1-500 GeV energy range. SEDs are plotted in equally spaced logarithmic bins from 100 MeV till the highest energy photon detected (data point or upper limit). The *prefactor* (normalization factor) of the four bright point sources within the ROI, as for the Galactic diffuse and isotropic models, were kept free in the likelihood optimization procedure, whereas all other parameters were fixed to the 3FGL values.

Spectral models of 3C 454.3 in the likelihood analysis were represented successively by the four functions indicated in Section 2, respectively PL, BPL, LP and PLEC, and defined in Eqs. (1, 2, 3, 4). The *Log(likelihood)* value is returned, corresponding to the best fit model parameters of the sources in the ROI and the source region. An upper limit is displayed when the number of photons, associated with 3C 454.3, as predicted by the model, $N_{pred} \leq 3$ or when *Test Statistic (TS)* ≤ 9. The so-obtained fitted functions were plotted above the SED data points, for the LP, BPL and PLEC models respectively. Results are presented in Fig. 5 and 6. The quality of unbinned fits is given by the $Log(likelihood)$ for each of these three fitting functions, and is reported in Table 5. The results of the spectral analysis were used to produce Fig. 3 (Section 4.1). We observe an overall good compatibility between the LP, BPL and PLEC models. Luminosity ($>$ 100 MeV) was also estimated, using the formula written in Eq. 6. A progressive hardening with the increase of flux is observed from Phase 1 to 3, at energies $E < E_{break}$, with Γ=2.43 ± 0.02, 2.26 ± 0.03, and 2.05 ± 0.01 respectively. Hardening of the spectrum is significant during Flare II, with $\Gamma = 2.00 \pm 0.02$, compared to $\Gamma = 2.11 \pm 0.02$ (PL model). To the best of our knowledge, Flare II represents the first extended phase when *Fermi*-LAT recorded such a hard spectrum during a major outburst of this source. The effect of this hardening can be seen on the parameters Γ_1, Γ_2 and α. We also fitted the data points with the same functions, but by including the model of absorption by the extragalactic background light (EBL) from Razzaque et al. (2009) and Finke et al. (2010). But none of our results were significantly changed.

We have also modeled an absorption pattern which includes the previously mentioned EBL along with absorption of γ rays in the broad line region (BLR) by the two photon pair production process, as described in Britto et al. (2015). No absorption feature was found, using a 6-line model of the BLR, but the sensitivity of *Fermi*-LAT in the range where the absorption could show up ($>$ 10 GeV) is too low within the few week duration of the outburst.

5. DISCUSSION

The 2014 May–July outburst of 3C 454.3 bore a flaring pattern typical of this FSRQ, namely a plateau, flare and post-flare phases, which was also observed during the previous three major γ-ray outbursts. The flux of 3C 454.3 reached an average value of $F_{100} = 7.2 \pm 0.2$ during the flaring phase of 2014 June 7–29, which is similar to the 2010 April flare but much weaker than the giant flare in 2010 November. The peak flux, $F_{100} = 21.6 \pm 2.6$ was recorded on 2014 June 15 (MJD 56823.5625) in a 3-hr light-curve. This corresponds to an isotropic-equivalent γ-ray luminosity of $L_\gamma \approx 6.2 \times 10^{49}$ erg s^{-1}, roughly an order of magnitude lower than the peak luminosity of the giant flare in 2010 November, but still quite substantial for a blazar. Therefore the jet opening angle should be $\theta_j \approx 3^\circ$ in order for the true luminosity $2(1 - \cos\theta_j)L_\gamma$ to be of the order of the accretion disc luminosity $L_d \approx 6.75 \times 10^{46}$ erg s^{-1} (Bonnoli et al. 2011). From VLBI observation, the jet opening angle is determined to be $0.^\circ 8 \pm 0.^\circ 2$ (Jorstad et al. 2005).

The 2014 June 7–29 flaring state of 3C 454.3 is characterized by several subflares with distinct peaks. An extremely fast rise of flux was recorded, on a time scale $T_r \approx 1000$ s, on MJD 56827. This is one of the shortest flux variability time measured for blazars in the GeV range. A few other subflares also show rapid, on hours time scale, flux rise. These variations could indicate γ rays being emitted from compact regions, namely blobs, in the jet. The radii of these blobs in the comoving frame, $R' \approx \delta c t_v/(1+z)$, depend on their Doppler factor δ and the time scale t_v over which their flux vary, *e.g.* Finke et al. (2008). A constraint on δ can be obtained by requiring the blob to be optically thin to high-energy photons against $\gamma\gamma \rightarrow e^\pm$ pair production process. In particular γ-rays of energy E_γ from 3C 454.3 should be interacting with $2m_e^2c^4\delta^2/E(1+z)^2 \approx 1.5(\delta/10)^2(E_\gamma/10\text{ GeV})^{-1}$ keV photons at threshold, if those X-ray photons are produced in the same blob. A more detailed calculation, following Gould & Schréder (1967), leads to an opacity formula

$$\tau_{\gamma\gamma}(E_\gamma) = \frac{\delta c t_v}{1+z}\pi r_0^2 \left[\frac{m_e^2c^4\delta}{(1+z)E_\gamma}\right]^2 \times \int_{\frac{m_e^2c^4\delta}{(1+z)E_\gamma}}^{\frac{(1+z)E_\gamma}{\delta}} \frac{n'(\epsilon')}{\epsilon'^2}\varphi[S_0(\epsilon')]d\epsilon', \quad (7)$$

for isotropic distribution of photons in the blob, where $\epsilon' = (1+z)\epsilon/\delta$ is the target photon energy in the blob frame and

$$n'(\epsilon') = \frac{(1+z)^2 d_L^2}{\delta^4 c^3 t_v^2}\, n\left(\frac{\delta\epsilon'}{1+z}\right)$$

is the target photon spectrum in the blob frame with $n(\epsilon)$ being the observed spectrum. The function $\varphi[S_0(\epsilon')]$, with $S_0(\epsilon') = (1+z)\epsilon' E_\gamma/\delta m_e^2 c^4$, is defined by Gould & Schréder (1967) and corrected by Brown et al. (1973). The condition $\tau_{\gamma\gamma}(E_\gamma) = 1$ can be translated to a lower limit on δ.

Swift-XRT observed 3C 454.3 during its 2014 June 7–29 flare. We analyzed public XRT data, using the procedure described in section 3. The flux level during the period MJD 56822– 56830 was observed to be almost constant, and was well fitted by a constant function $p_0 = (2.06 \pm 0.95) \times 10^{-11}$ in the 2–6 keV range. This period coincides with the γ-ray subflares: Peak 3, Peak 4 and Peak 5, respectively as denoted in Fig. 2. The value of the p_0 parameter and its error were plotted as the XRT data point on the SED of each of these peaks. These subflares also contain a 12 GeV (Peak 3), a 43 GeV (Peak 4) and a 35 GeV (Peak 5) photon, detected with high confidence. To constrain the Doppler factor δ, we fit LAT and XRT data together, giving the best-fit to be log-parabola during Peak 3 and Broken Power-Law during Peak 4 and Peak 5, assuming γ-ray and X-ray originated from the same blob during those two subflares. Assuming that the flux variability time is $t_v = T_r = 1.4$ hr for Peak 3, 0.3 hr (1000 sec) for Peak 4, and 23.8 hr for Peak 5, we calculate $\delta \gtrsim 20$, 31 and 14, respectively, requiring the $\gamma\gamma$ opacity for the 12 GeV, 43 GeV and 35 GeV photons are less than or equal to 1 according to Eq. (7). (We also got a good fit of the Peak 4 SED by using a log-parabola function, which gave a similar value $\delta \gtrsim 30$.) While the δ values for Peak 3 and Peak 5 are similar to the ones obtained for the 2010 November flare, the value $\delta \gtrsim 31$ for Peak 4 is higher and is particularly interesting. Using an angle 1.3° between the jet and our line of sight, inferred as an average value from long-term Very Long Baseline Interferometry (VLBI) (Jorstad et al. 2005), and $\delta = [\Gamma_{\rm jet}(1-\beta_{\rm jet}\cos\theta)]^{-1} \simeq 31$ we calculate the jet Lorentz factor $\Gamma_{\rm jet} \simeq 18$. This is compatible with the previously estimated value of $\Gamma_{\rm jet} \simeq 16$ reported by Jorstad et al. (2005), and is equal to the value estimated in Sikora et al. (2008).

The distances of the γ-ray emitting blobs from the central black hole can be calculated, using the minimum Doppler factor derived from the $\gamma\gamma$ opacity condition and the resulting minimum jet Lorentz factor, as $r \simeq 2\Gamma_{\rm jet}^2 c t_v/(1+z)$. For the Peak 3, Peak 4 and Peak 5 data this would imply distances $r \gtrsim 1.6 \times 10^{16}$ cm, $\gtrsim 1.0 \times 10^{16}$ cm and $\gtrsim 1.4 \times 10^{17}$ cm, respectively. These progressively larger distances have implications for high-energy γ-ray emission. Interestingly indeed, significant emission above 10 GeV took place during the later part of the flare, in particular during Peak 3 and later (see Fig. 2). In the context of multiple γ-ray emitting blobs for different Peaks in the LAT light-curve, blobs which are slower and optically thick to $\gamma\gamma$ pair production would emit little or no high-energy photons. This could be the case for Peak 1 and Peak 2. On the other hand, as we have also derived from the $\gamma\gamma$ opacity condition previously for Peak 3, Peak 4 and Peak 5, the blobs which are faster and optically thin to $\gamma\gamma$ pair production would emit significant high-energy photons.

Absorption of $\gtrsim 10$ GeV photons, due to $\gamma\gamma \to e^{\pm}$ pair production process in the BLR with line and continuum photons, has been suggested as a plausible explanation of spectral break in the blazar SEDs. While we do find spectral breaks at $\sim$ 1-2 GeV for all phases (see Figs. 5 and 6), compatible with previous outbursts of 3C 454.3, our fits do not improve significantly when we include absorption using a BLR model with 6 of the strongest lines (Britto et al. 2015). This could imply that the γ-ray emission region is located close to the outer edge of the BLR, as is also implied by the constraints on the Doppler factor.

ACKNOWLEDGMENTS

We thank Justin Finke for his meticulous reading of the draft and valuable comments.

The *Fermi*-LAT Collaboration acknowledges generous ongoing support from a number of agencies and institutes that have supported both the development and the operation of the LAT as well as scientific data analysis. These include the National Aeronautics and Space Administration and the Department of Energy in the United States, the Commissariat à l'Energie Atomique and the Centre National de la Recherche Scientifique / Institut National de Physique Nucléaire et de Physique des Particules in France, the Agenzia Spaziale Italiana and the Istituto Nazionale di Fisica Nucleare in Italy, the Ministry of Education, Culture, Sports, Science and Technology (MEXT), High Energy Accelerator Research Organization (KEK) and Japan Aerospace Exploration Agency (JAXA) in Japan, and the K. A. Wallenberg Foundation, the Swedish Research Council and the Swedish National Space Board in Sweden.

Additional support for science analysis during the operations phase is gratefully acknowledged from the Istituto Nazionale di Astrofisica in Italy and the Centre National d'Études Spatiales in France.

E.B. acknowledges NASA grants NNX13AO84G and NNX13AF13G.

R. J. G. B. and S. R. acknowledge support from the National Research Foundation, South Africa and the South African Gamma-ray Astronomy Programme (SAGAMMA).

REFERENCES

Abdo, A. A., Ackermann, M., Ajello, M., et al. 2009, ApJ, 699, 817
—. 2010, ApJ, 710, 1271
—. 2011, ApJ, 733, L26
Acero, F., Ackermann, M., Ajello, M., et al. 2015, ApJS, 218, 23
Ackermann, M., Ajello, M., Baldini, L., et al. 2010, ApJ, 721, 1383
Ackermann, M., Ajello, M., Albert, A., et al. 2012, ApJS, 203, 4
Arnaud, K. A. 1996, in Astronomical Data Analysis Software and Systems V, Vol. 101, Astronomical Society of the Pacific Conference Series, ed. G. H. J. . J. Barnes, 17

Atwood, W. B., Abdo, A. A., Ackermann, M., et al. 2009, ApJ, 697, 1071
Bevington, P. R., & Robinson, D. K. 1992, Data reduction and error analysis for the physical sciences, ed. n. e. New York: McGraw-Hill, —c1992
Bonnoli, G., Ghisellini, G., Foschini, L., Tavecchio, F., & Ghirlanda, G. 2011, MNRAS, 410, 368
Bregeon, J., Charles, E., & M. Wood for the Fermi-LAT collaboration. 2013, ArXiv e-prints, arXiv:1304.5456
Britto, R. J. G., Razzaque, S., Lott, B., & on behalf of the Fermi-LAT Collaboration. 2015, ArXiv e-prints, arXiv:1502.07624
Brown, R. W., Mikaelian, K. O., & Gould, R. J. 1973, Astrophys. Lett., 14, 203
Carrasco, L., Gonzalez, R., Porras, A., et al. 2014, The Astronomer's Telegram, 6213, 1
Cerruti, M., Dermer, C. D., Lott, B., Boisson, C., & Zech, A. 2013, ApJ, 771, L4
Chandra, S., Baliyan, K. S., Matta, S., & Prabhu, D. S. 2014, The Astronomer's Telegram, 6232, 1
Dotson, A., Georganopoulos, M., Kazanas, D., & Perlman, E. S. 2012, ApJ, 758, L15
Finke, J. D., & Dermer, C. D. 2010, ApJ, 714, L303
Finke, J. D., Dermer, C. D., & Böttcher, M. 2008, ApJ, 686, 181
Finke, J. D., Razzaque, S., & Dermer, C. D. 2010, ApJ, 712, 238
Fuhrmann, L., Larsson, S., Chiang, J., et al. 2014, MNRAS, 441, 1899
Gould, R. J., & Schréder, G. P. 1967, Physical Review, 155, 1408
Hartman, R. C., Bertsch, D. L., Bloom, S. D., et al. 1999, ApJS, 123, 79
Hunger, L., & Reimer, A. 2015, in ICRC 2015, Vol. 910, Proceedings of Science
Jorstad, S. G., Marscher, A. P., Lister, M. L., et al. 2005, AJ, 130, 1418
Jorstad, S. G., Marscher, A. P., Larionov, V. M., et al. 2010, ApJ, 715, 362
Jorstad, S. G., Marscher, A. P., Smith, P. S., et al. 2013, ApJ, 773, 147
Kalberla, P. M. W., Burton, W. B., Hartmann, D., et al. 2005, A&A, 440, 775
Kohler, S., & Nalewajko, K. 2015, MNRAS, 449, 2901
Lott, B., Escande, L., Larsson, S., & Ballet, J. 2012, A&A, 544, A6
Lynds, C. R. 1967, ApJ, 147, 837
MacPherson, E., Hasan, I., Urry, M., et al. 2014, The Astronomer's Telegram, 6266, 1
Mena, O., & Razzaque, S. 2013, JCAP, 11, 23
Moretti, A., Campana, S., Tagliaferri, G., et al. 2004, in Society of Photo-Optical Instrumentation Engineers (SPIE) Conference Series, Vol. 5165, X-Ray and Gamma-Ray Instrumentation for Astronomy XIII, ed. K. A. Flanagan & O. H. W. Siegmund, 232–240
Nalewajko, K., Begelman, M. C., & Sikora, M. 2014, ApJ, 789, 161
Nolan, P. L., Abdo, A. A., Ackermann, M., et al. 2012, ApJS, 199, 31
Orienti, M., Koyama, S., D'Ammando, F., et al. 2013, MNRAS, 428, 2418
Pacciani, L., Tavecchio, F., Donnarumma, I., et al. 2014, ApJ, 790, 45
Pacciani, L., Vittorini, V., Tavani, M., et al. 2010, ApJ, 716, L170
Planck Collaboration, Ade, P. A. R., Aghanim, N., et al. 2014, A&A, 571, A16
Poutanen, J., & Stern, B. 2010, ApJ, 717, L118
Razzaque, S., Dermer, C. D., & Finke, J. D. 2009, ApJ, 697, 483
Sikora, M., Moderski, R., & Madejski, G. M. 2008, ApJ, 675, 71
Stern, B. E., & Poutanen, J. 2011, MNRAS, 417, L11
—. 2014, ApJ, 794, 8
Striani, E., Vercellone, S., Tavani, M., et al. 2010, ApJ, 718, 455
Tachibana, Y., Kawai, N., Pike, S., for the MAXI team, & the MITSuME team. 2015, ArXiv e-prints, arXiv:1502.03610
Vercellone, S., Chen, A. W., Vittorini, V., et al. 2009, ApJ, 690, 1018
Vercellone, S., D'Ammando, F., Vittorini, V., et al. 2010, ApJ, 712, 405
Verrecchia, F., Lucarelli, F., Pittori, C., et al. 2014, The Astronomer's Telegram, 6182, 1

TABLE 1
3C 454.3 SOFT X-RAY SPECTRAL FIT.

XRT obs. (*id* | *modes*)	start (*date*)	expo (*sec*)	Γ	Γ_{hard}	E_{break} (*keV*)	norm (10^{-3} *ph keV*$^{-1}$ *cm*$^{-2}$)	χ^2	d.o.f.	flux 2–6 keV (10^{-11} *erg cm*$^{-2}$ *s*$^{-1}$)
00031018014 WT	2014-Jun-14 06:23:59	3965	$1.44^{1.49}_{1.38}$	...	...	$6.28^{6.55}_{6.01}$	96.52	123	$2.23^{2.29}_{2.16}$
00031018016 PC	2014-Jun-16 14:20:58	2988	$1.54^{1.60}_{1.48}$	...	...	$6.78^{7.12}_{6.44}$	90.56	94	$2.10^{2.17}_{2.04}$
00031018017 WT	2014-Jun-17 16:10:59	1793	$1.91^{2.02}_{1.80}$	...	...	$8.57^{9.14}_{8.01}$	53.60	51	$1.66^{1.77}_{1.57}$
00031018019 WT	2014-Jun-18 03:09:59	1584	$2.33^{2.53}_{2.15}$	$1.53^{1.68}_{1.38}$	$1.62^{1.88}_{1.40}$	$9.18^{9.66}_{8.69}$	65.51	67	$1.97^{2.01}_{1.89}$
00031018020 WT	2014-Jun-21 14:19:59	1684	$2.47^{2.60}_{2.34}$	$1.76^{1.86}_{1.65}$	$1.53^{1.74}_{1.38}$	$22.38^{23.18}_{21.60}$	142.66	133	$3.86^{4.01}_{3.75}$

TABLE 2
OUTBURST PHASES OF 3C 454.3, AS IDENTIFIED FROM THE LIGHT-CURVES.

	Phase	Dates	MJD	Duration (days)
1	Pre-flare	2013 Oct 5 - 2014 May 20	56570.0 - 56797.0	227.0
2	Plateau	2014 May 20 - 2014 Jun 7	56797.0 - 56815.0	18.0
3	Flare	2014 Jun 7 - 2014 Jun 29	56815.0 - 56837.0	22.0
4	Post-flare	2014 Jun 29 - 2014 Jul 25	56837.0 - 56863.0	26.0
3a	Flare I	2014 Jun 10 - 18 Jun	56818.5 - 56826.5	8.0
3b	Flare II	2014 Jun 20 - 25 Jun	56828.0 - 56833.5	5.5

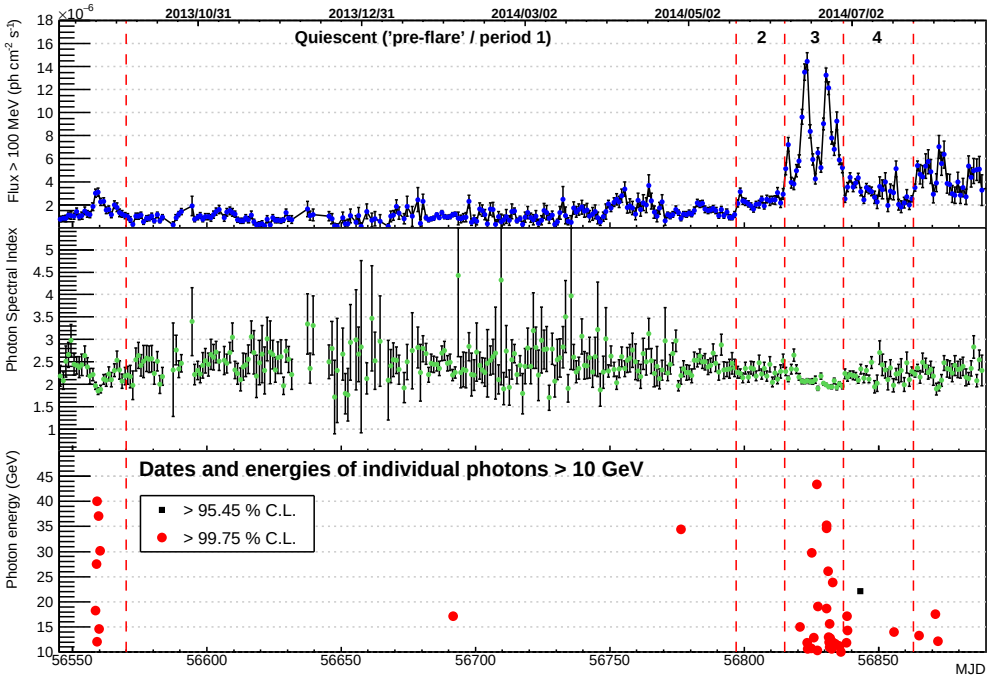

FIG. 1.— *Top panel: Fermi*-LAT light-curve of 3C 454.3 from 2013 August to 2014 August, including the 2013 September 23–25 flare, the 2013 October 5-2014 May 20 pre-flare (phase 1) and the 2014 May–July outburst (phases 2, 3, 4), with 1-day binning. Gaps appeared in the light-curve during the pre-flare due to low-exposure modes. *Middle panel:* Photon index (Γ) versus time. *Bottom panel:* Time of arrival of E>10 GeV photons with two different significance levels of source association (2- and 3-σ Gaussian equivalent). Vertical dashed lines separate the four phases studied.

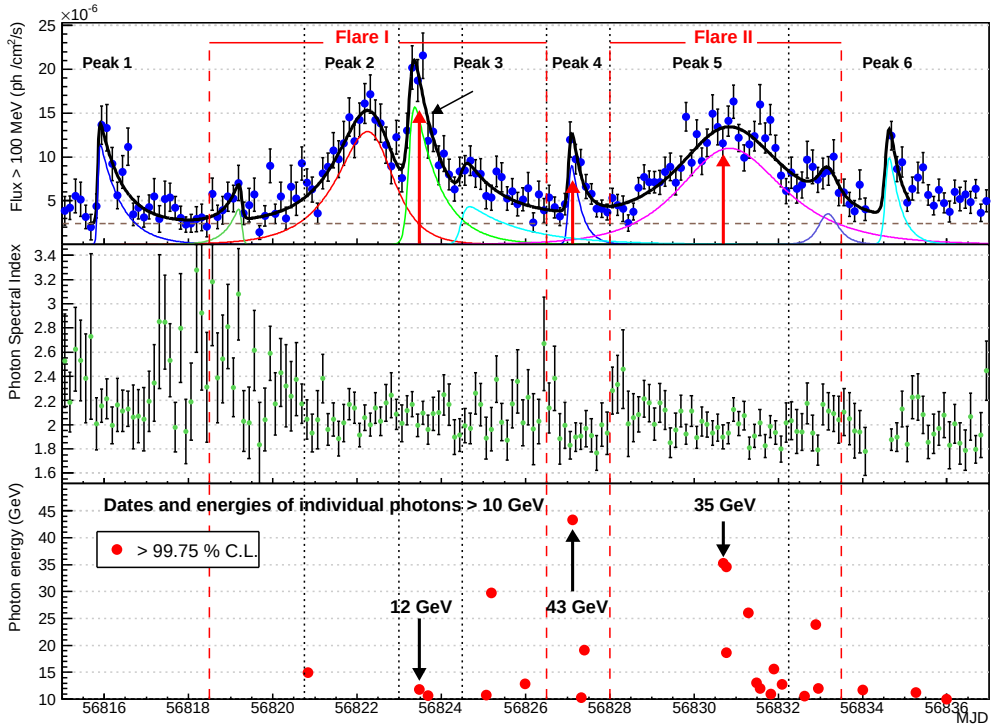

FIG. 2.— (Top panel) *Fermi*-LAT light-curve of the flare phase with 3-hr binning. Flaring peaks were fitted by the F function (in Eq. 5) for 9 structures. Fits were performed in the MJD 56815.625-56835.130 time range. The thin color lines correspond to the contribution of single peaks in the total fit, which is represented by the thick black line. The dashed brown line is the fitted constant baseline, which also contributes to the total fit. Six major peaks were labeled for more detailed studies. The red arrows indicate the arrival time of the three high-energy photons used to calculate the Doppler factor in section 5 (Discussion), and whose energies are labeled in the bottom panel. Due to an instrumental problem, the MJD 56834.375 bin contains no data. *Middle panel:* Photon spectral index (Γ) of the PL fits of data. *Bottom panel:* Photons above 10 GeV with a 0.9975 % probability in the significance level of source association (3-σ Gaussian equivalent). This panel is a zoom of the bottom panel of Fig. 1. Vertical red dash lines indicate the two major flaring phases (I and II), and black dotted lines Peaks 2, 3, 4 and 5.

TABLE 3
PARAMETERS OF FIT FUNCTION F, FOR THE 6 PEAKS IDENTIFIED IN FIG. 2.

Peak	t_0 (MJD)	F_0 (10^{-6} $ph\ cm^{-2}\ s^{-1}$)	T_r (hr)	T_f (hr)
1	56815.8477	6.6 ± 1.1	0.5 ± 0.1	12.6 ± 2.8
2	56822.3984	12.5 ± 0.9	18.4 ± 1.9	11.0 ± 1.8
3	56823.2422	10.5 ± 1.5	1.4 ± 0.7	15.1 ± 2.3
4	56827.0391	6.7 ± 1.3	0.9 ± 0.5	5.6 ± 1.1
5	56830.7305	10.9 ± 0.6	23.8 ± 1.9	29.2 ± 2.6
6	56834.5625	7.5 ± 0.5	1.1 ± 1.0	6.6 ± 2.1

Note. A constant baseline flux of $(2.4 \pm 0.6) \times 10^{-6}$ $ph\ cm^{-2}\ s^{-1}$ was also fitted to the data. The χ^2/ndf for the whole fit is $145.7/115 = 1.27$.

TABLE 4
PARAMETERS OF THE PL, BPL, LP AND PLEC FIT FUNCTIONS OBTAINED BY THE LIKELIHOOD ANALYSIS FOR PEAKS 2, 3, 4 AND 5.

PL	date	$F[>100MeV]$		Γ			$-Log(likelihood)$
	(MJD)	$(10^{-6}\ photons\ cm^{-2}\ s^{-1})$					
Peak 2	56820.75-56823.00	11.1 ± 0.5		2.06 ± 0.03			10093.1
Peak 3	56823.00-56824.50	12.4 ± 0.6		2.08 ± 0.04			7181.1
Peak 4	56826.50-56828.00	5.8 ± 0.4		1.94 ± 0.04			5858.4
Peak 5	56828.00-56832.25	9.7 ± 0.3		2.00 ± 0.02			23202.7
BPL	date	$F[>100MeV]$	Luminosity	Γ_1	Γ_2	E_{break}	$\Delta\ Log(likelihood)$
	(MJD)	$(10^{-6}\ photons\ cm^{-2}\ s^{-1})$	$(10^{48}\ erg\ s^{-1})$				
Peak 2	56820.75-56823.00	10.3 ± 0.5	28.3	1.85 ± 0.06	2.40 ± 0.09	1000 ± 100	−11.4
Peak 3	56823.00-56824.50	11.7 ± 0.6	29.9	1.93 ± 0.06	2.50 ± 0.14	1500 ± 100	−6.8
Peak 4	56826.50-56828.00	5.4 ± 0.4	19.4	1.78 ± 0.07	2.39 ± 0.17	1900 ± 200	−1.7
Peak 5	56828.00-56832.25	9.1 ± 0.3	28.9	1.79 ± 0.04	2.28 ± 0.05	1000 ± 100	−22.7
LP	date	$F[>100MeV]$	Luminosity	α	β		$\Delta\ Log(likelihood)$
	(MJD)	$(10^{-6}\ photons\ cm^{-2}\ s^{-1})$	$(10^{48}\ erg\ s^{-1})$				
Peak 2	56820.75-56823.00	10.1 ± 0.5	26.9	1.81 ± 0.06	0.12 ± 0.03		−13.8
Peak 3	56823.00-56824.50	11.6 ± 0.6	30.8	1.91 ± 0.07	0.08 ± 0.03		−5.0
Peak 4	56826.50-56828.00	5.4 ± 0.4	20.4	1.75 ± 0.09	0.08 ± 0.03		−3.9
Peak 5	56828.00-56832.25	9.0 ± 0.3	27.8	1.76 ± 0.04	0.11 ± 0.02		−28.5
PLEC	date	$F[>100MeV]$	Luminosity	Γ_{PLEC}	E_{cutoff}		$\Delta\ Log(likelihood)$
	(MJD)	$(10^{-6}\ photons\ cm^{-2}\ s^{-1})$	$(10^{48}\ erg\ s^{-1})$				
Peak 2	56820.75-56823.00	10.4 ± 0.5	25.6	1.84 ± 0.06	6700 ± 1800		−14.8
Peak 3	56823.00-56824.50	11.8 ± 0.6	28.8	1.93 ± 0.06	10500 ± 4200		−6.5
Peak 4	56826.50-56828.00	5.5 ± 0.4	19.3	1.81 ± 0.07	16300 ± 7900		−4.5
Peak 5	56828.00-56832.25	9.3 ± 0.3	26.9	1.83 ± 0.03	10800 ± 2200		−25.6

TABLE 4 **Note.** These parameters are defined in Eq. 1-4. The quality of unbinned fits is given by the $Log(likelihood)$ for each of these three fitting functions, for the PL model, along with other fit parameters. For the LP, BPL and PLEC models, values of $\Delta Log(likelihood)$ are given, with respect to $Log(likelihood)$ of the PL fit. Luminosity was estimated according to the formula of Eq. 6.

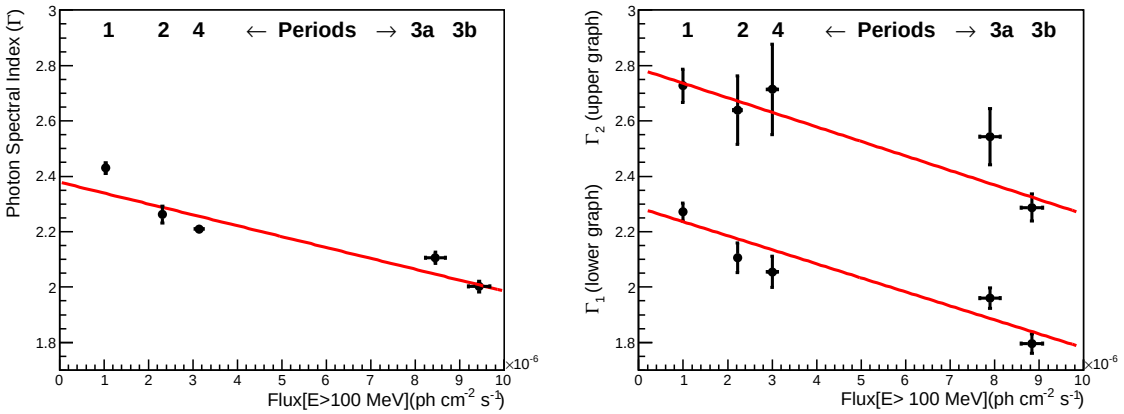

FIG. 3.— Photon spectral index *versus* F_{100} for five phases of the outburst: pre-flare, plateau, flare I, flare II and post-flare, as defined in Table 2. Left panel: Fluxes are calculated with PL model of photon index Γ. Right panel: Fluxes are calculated with BPL model of photon indices Γ_1 and Γ_2.

TABLE 5
Parameters of the PL, BPL, LP and PLEC functions fitted to the spectra for the pre-flare and different phases of the 2014 May–July outburst.

PL	date (MJD)	$F[>100MeV]$ (10^{-6} $photons\ cm^{-2}\ s^{-1}$)	Luminosity (10^{48} $erg\ s^{-1}$)	Γ			$-Log(likelihood)$
Pre-flare (1)	56570.0-56797.0	1.04 ± 0.02	1.5	2.43 ± 0.02			277115.8
Plateau (2)	56797.0-56815.0	2.3 ± 0.1	4.5	2.26 ± 0.03			35867.2
Flare (3)	56815.0-56837.0	7.7 ± 0.1	25.3	2.05 ± 0.01			84030.2
Post-flare (4)	56837.0-56863.0	3.1 ± 0.1	6.9	2.21 ± 0.02			42526.9
Flare I (3a)	56818.5-56826.5	8.5 ± 0.2	24.0	2.11 ± 0.02			29689.5
Flare II (3b)	56828.0-56833.5	9.4 ± 0.2	35.4	2.00 ± 0.02			28040.5
BPL	date (MJD)	$F[>100MeV]$ ($photons\ cm^{-2}\ s^{-1}$)	Luminosity (10^{48} $erg\ s^{-1}$)	Γ_1	Γ_2	E_{break}	Δ $Log(likelihood)$
Pre-flare (1)	56570.0-56797.0	0.99 ± 0.02	1.3	2.29 ± 0.03	2.80 ± 0.07	$100\ ^{+200}_{-200}$	−20.9
Plateau (2)	56797.0-56815.0	2.2 ± 0.1	3.7	2.18 ± 0.03	4.63 ± 0.73	$4200\ ^{+3500}_{-700}$	−14.7
Flare (3)	56815.0-56837.0	7.3 ± 0.1	19.5	1.92 ± 0.02	2.57 ± 0.05	$2000\ ^{+300}_{-200}$	−70.7
Post-flare (4)	56837.0-56863.0	3.0 ± 0.1	5.5	2.08 ± 0.03	3.04 ± 0.16	$2100\ ^{+1800}_{-200}$	−21.2
Flare I (3a)	56818.5-56826.5	8.0 ± 0.2	18.8	1.98 ± 0.03	2.66 ± 0.10	$2000\ ^{+300}_{-300}$	−23.7
Flare II (3b)	56828.0-56833.5	8.9 ± 0.2	26.9	1.85 ± 0.03	2.47 ± 0.08	$1800\ ^{+700}_{-300}$	−28.9
LP	date (MJD)	$F[>100MeV]$ ($photons\ cm^{-2}\ s^{-1}$)	Luminosity (10^{48} $erg\ s^{-1}$)	α	β		Δ $Log(likelihood)$
Pre-flare (1)	56570.0-56797.0	0.98 ± 0.02	1.3	2.30 ± 0.03	0.10 ± 0.02		−19.7
Plateau (2)	56797.0-56815.0	2.2 ± 0.1	3.8	2.09 ± 0.05	0.12 ± 0.03		−11.7
Flare (3)	56815.0-56837.0	7.1 ± 0.1	19.7	1.84 ± 0.02	0.10 ± 0.01		−72.8
Post-flare (4)	56837.0-56863.0	3.0 ± 0.1	5.7	2.03 ± 0.04	0.11 ± 0.02		−16.8
Flare I (3a)	56818.5-56826.5	7.9 ± 0.2	19.3	1.92 ± 0.04	0.09 ± 0.02		−20.8
Flare II (3b)	56828.0-56833.5	8.7 ± 0.2	26.7	1.77 ± 0.04	0.10 ± 0.02		−32.2
PLEC	date (MJD)	$F[>100MeV]$ ($photons\ cm^{-2}\ s^{-1}$)	Luminosity (10^{48} $erg\ s^{-1}$)	Γ_{PLEC}	E_{cutoff}		Δ $Log(likelihood)$
Pre-flare (1)	56570.0-56797.0	1.0 ± 0.02	1.3	2.28 ± 0.03	6500 ± 1400		−19.6
Plateau (2)	56797.0-56815.0	2.2 ± 0.1	3.6	2.05 ± 0.06	4800 ± 1300		−14.8
Flare (3)	56815.0-56837.0	7.3 ± 0.1	18.9	1.89 ± 0.02	10000 ± 1200		−72.2
Post-flare (4)	56837.0-56863.0	3.0 ± 0.1	5.5	2.04 ± 0.04	6800 ± 1600		−17.0
Flare I (3a)	56818.5-56826.5	8.0 ± 0.2	18.3	1.94 ± 0.04	9100 ± 1900		−23.5
Flare II (3b)	56828.0-56833.5	9.0 ± 0.2	25.8	1.84 ± 0.03	10900 ± 2100		−29.4

TABLE 5 **Note.** These parameters are defined in Eq. 1-4. The quality of unbinned fits is given by the $Log(likelihood)$ for each of these three fitting functions, for the PL model, along with other fit parameters. For the LP, BPL and PLEC models, values of $\Delta Log(likelihood)$ are given, with respect to $Log(likelihood)$ of the PL fit. Luminosity was estimated according to the formula of Eq. 6.

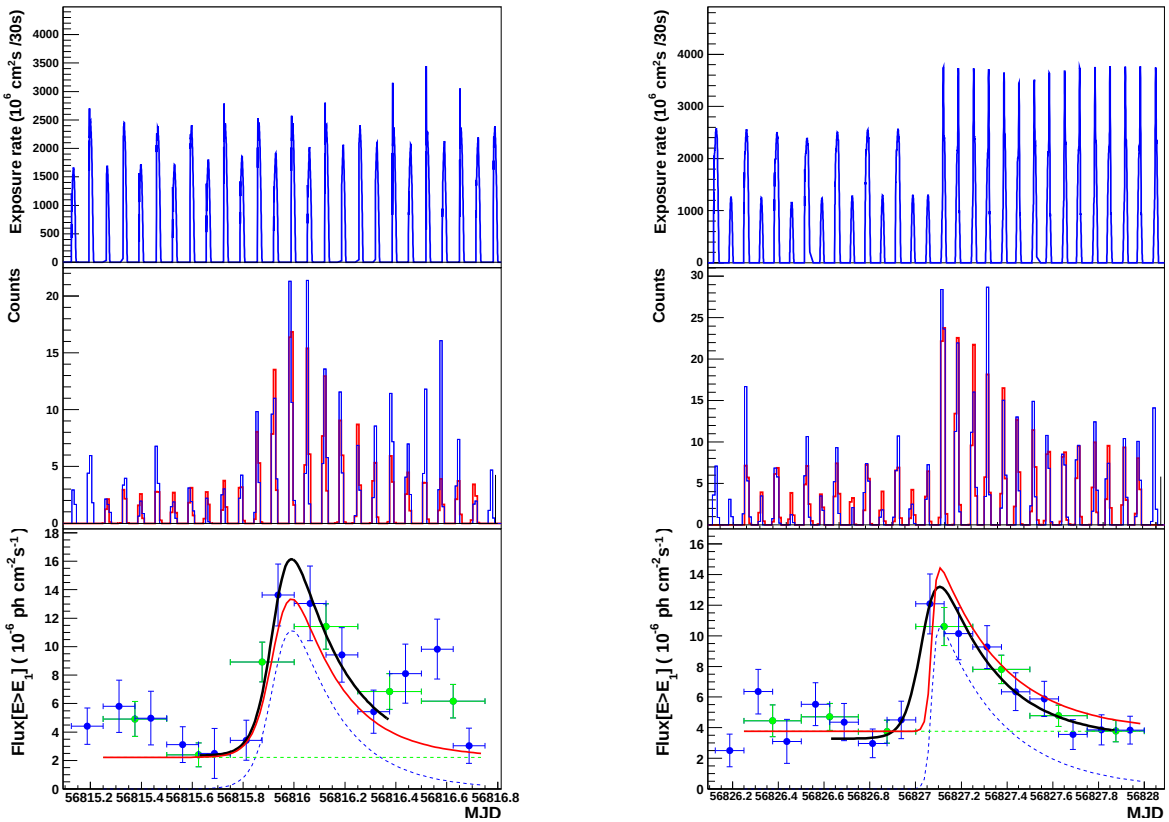

FIG. 4.— Left panel: MJD 56816 ("peak 1") flare. Top panel: Exposure rate as a function of time. Middle panel: Measured (probability-weighted, blue) and modeled (red) photon counts. Bottom panel: light-curves. Blue points: 3-hr binning, green points: 6 hr-binning. Black curve: function fitted to 3-hr points. Red curve: function fitted using the unbinned method. The green dashed line corresponds to the continuous component and the blue one to the flare component $F(t)$ given in Eq. 5. Right: Same for the MJD 56827 ("peak 4") flare.

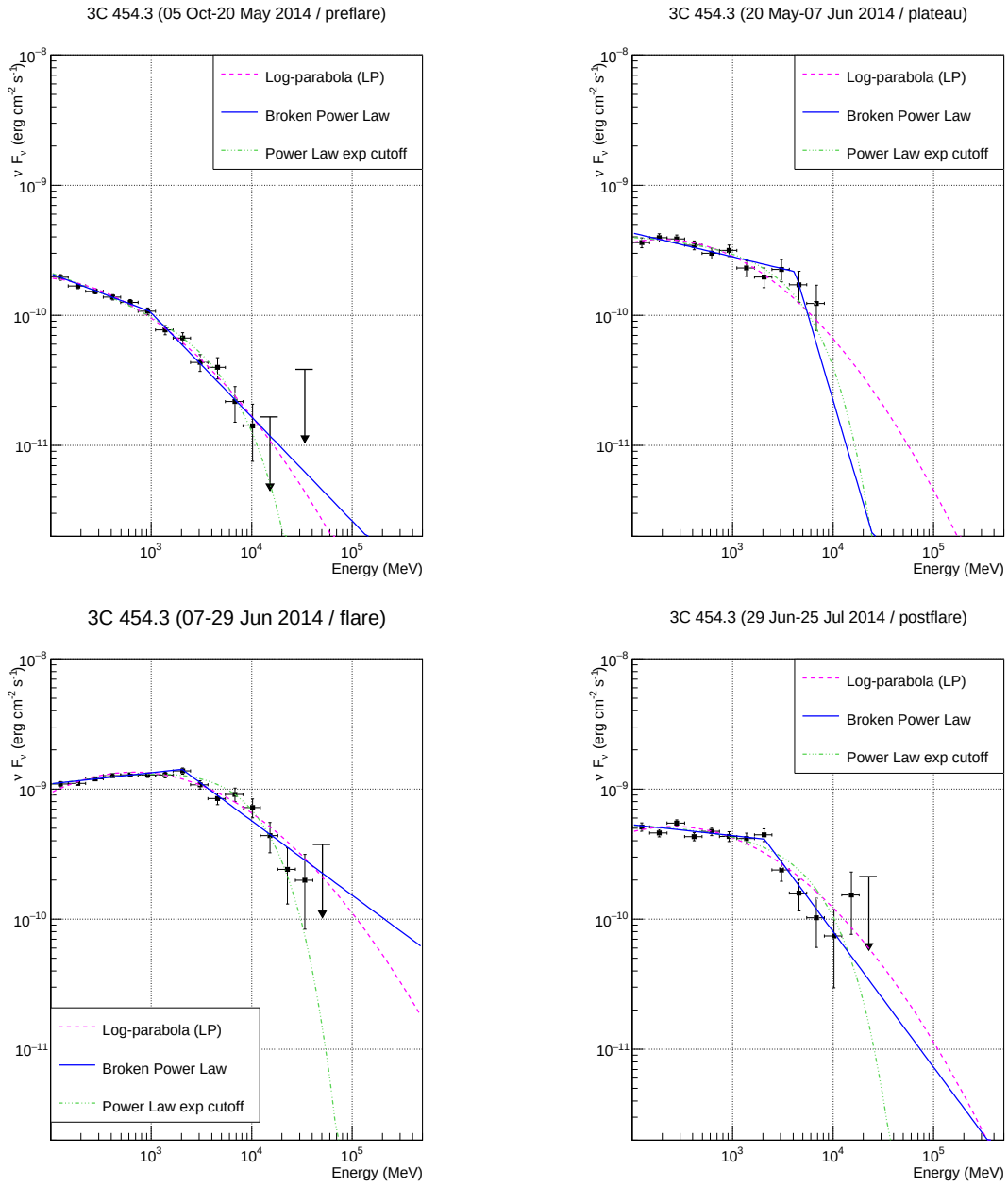
3C 454.3 (05 Oct-20 May 2014 / preflare)
3C 454.3 (20 May-07 Jun 2014 / plateau)
3C 454.3 (07-29 Jun 2014 / flare)
3C 454.3 (29 Jun-25 Jul 2014 / postflare)
Log-parabola (LP)
Broken Power Law
Power Law exp cutoff
ν F_ν (erg cm^-2 s^-1)
Energy (MeV)

FIG. 5.— Spectral energy distributions of 3C 454.3 above 100 MeV for the pre-flare, plateau, flare and post-flare phases, along with the LP, BPL and PLEC fitted functions.

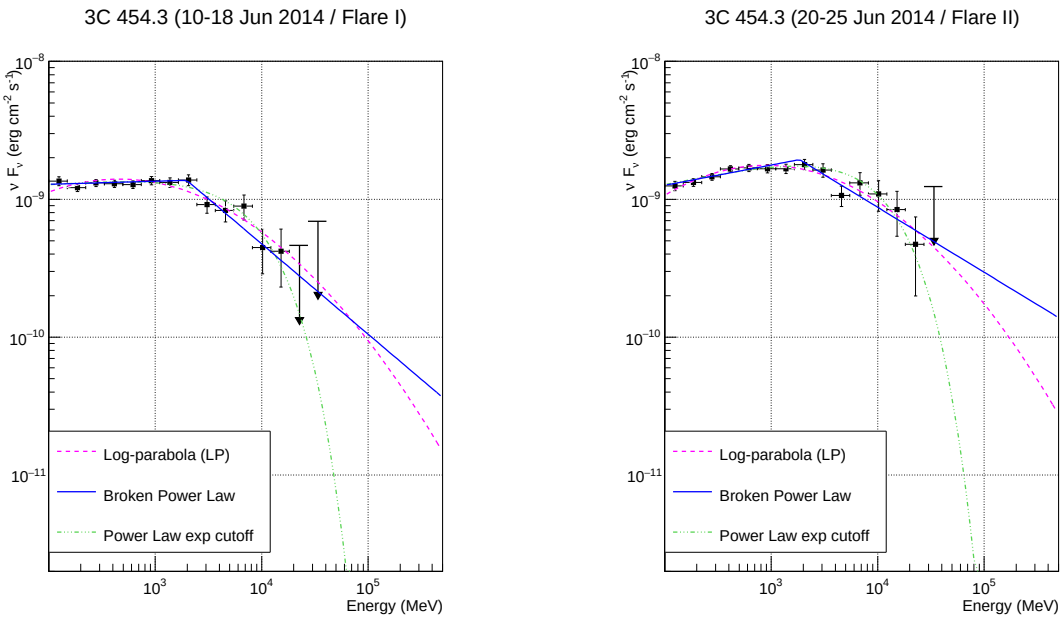
3C 454.3 (10-18 Jun 2014 / Flare I)
3C 454.3 (20-25 Jun 2014 / Flare II)
ν F_ν (erg cm^-2 s^-1)
Energy (MeV)
Log-parabola (LP)
Broken Power Law
Power Law exp cutoff

FIG. 6.— Spectral energy distributions of 3C 454.3 above 100 MeV for the two major peaks (Flare I and II) of the flare phase, along with the LP, BPL and PLEC fitted functions.